UCRL- 102861
PREPRINT

Southern Oscillation in the OSU Coupled Upper Ocean/Atmosphere GCM

Kenneth R. Sperber, Sultan Hameed,
W. Lawrence Gates and Gerald L. Potter

This paper was prepared for submission to the
14th Annual Climate Diagnostics Workshop,
held at the Scripps Institution of Oceanography
October 16–20, La Jolla, CA

January 1990

Southern Oscillation in the OSU Coupled Upper Ocean/Atmosphere GCM

Kenneth R. Sperber
[1]*Lawrence Livermore National Laboratory*
P.O. Box 808, L-264, Livermore, CA 94550

UCRL--102861

Sultan Hameed
Institute for Atmospheric Sciences, State University of New York
Stony Brook, NY 11794-2300

DE90 008415

W. Lawrence Gates[1] and Gerald L. Potter[1]

1. Introduction: With the advent of coupled ocean/atmosphere global climate models it has become possible to study their inherent natural variability. This natural variability arises as a consequence of the encoded physics and dynamics since the only imposed constraint on the simulation is the diurnal and annual cycle of solar radiation. One of the dominant modes of interannual variability is the Southern Oscillation (SO). The Oregon State University coupled upper ocean/atmosphere global climate model has been shown to qualitatively simulate many aspects of the SO (Sperber *et al.* 1987; Sperber, 1989). Sea-level pressure (SLP), sea-surface temperature (SST), thermocline layer temperature, surface air temperature, precipitation, and mixed layer currents are among the simulated fields which reproduce SO characteristics. Thus the nature of ocean/atmosphere feedback processes can be investigated.

The primary signature of the SO is a large-scale variation of SLP and SST across the tropical Pacific Ocean. This variation results in anomalous weather conditions over much of the globe. Of immediate interest is the evolution of SST anomalies during extreme phases of the SO. During the low phase the southeast tradewind system is weaker than normal or may even reverse. Associated with this breakdown of the trans-Pacific pressure gradient are anomalously warm SST anomalies, usually on the order of several °C. These extreme warmings, El Niño events, are *typically* characterized by westward propagation of SST anomalies from the coast of South America beginning early in the calander year of onset. Towards the end of the year these anomalies merge with those propagating from the western Pacific (Rasmusson and Carpenter, 1982). Thus, these events usually occur in phase with the seasonal cycle. *Atypical* events, such as the 82/83 and 86/87 El Niños, evolve out of phase with the seasonal cycle. That is, eastward propagation of SST anomalies from the western Pacific dominates, with the warm anomalies in the eastern Pacific not developing until late northern summer and early fall.

2. Evolution of Trans-Pacific SST Anomalies: GCM simulated composite monthly SST anomaly maps for warm episodes (low Southern Oscillation Index) have been generated. These provide the time sequence of the spatial evolution of SST anomalies in the region 130°E-70°W, 30°S-30°N. Due to space limitations it is not possible to present the monthly composites for the whole event. Rather, averages of selected months that capture the essence of the temporal evolution will be presented. These are shown in Figures 1a-d. This may be compared with the temporal evolution of SST anomalies presented in Rasmusson and Carpenter (1982) based upon the composite evolution for the 1951, 1953, 1957, 1965, 1969,

and 1972 El Niños. Following the notation of Rasmusson and Carpenter (1982) we denote months of the year during which the maximum SST anomaly in the eastern Pacific occurs with (0) and months during the subsequent year with (+1) respectively.

In the early spring [March(0) and April(0)], see Figure 1a, the simulated SST anomalies adjacent to South America reach their maximum values corresponding to the timing found by Rasmusson and Carpenter (1982). Subsequent evolution of the model warm event in the eastern Pacific departs from the *typical* scenario previously outlined. Rather, development mimics the evolution of the *atypical* event. During early summer, [May(0), June(0), and July(0)], see Figure 1b, the spatial extent of the 0.2°C isotherm in the western Pacific increases with anomalies $\geq$ 0.4°C now located near 150°W. In the monthly anomalies, not shown, the SST anomalies in the eastern Pacific became negative during May(0) and June(0) with out of phase positive anomalies developing during July(0). Rapid growth of anomalous conditions occurs during late summer and early fall. By August(0) the eastern and western 0.2°C isotherms merge, resulting in SST anomalies of $\geq$ 0.2°C that span the tropical basin from South America to Indonesia. From September(0) through November(0) the strength of the anomalies continues to enhance throughout the basin. The resulting mean August(0), September(0), October(0), and November(0) anomalous distribution is given in Figure 1c. The largest SST anomalies of the warm event, ~0.9°C, occur near the equator at 115°W during October(0). Thus, the model warm event reaches its mature phase somewhat earlier than seen in observations, which show the greatest extent of the warm anomalies between November (0) and January (+1) after onset (Rasmusson and Carpenter, 1982; Philander, 1983). The location of the simulated maximum is adjacent to the location of the negative node of the annually averaged SLP isocorrelation seen in Sperber *et al.* (1987) which characterizes the primary atmospheric signature of the SO. The subsequent decay of the positive anomalies in the model also occurs earlier than has been observed. In the December(0), January(+1), and February(+1) composite, Figure 1d, the model warm event has decayed with anomalies of $\sim$ 0.2°C spanning most of the tropical and subtropical Pacific.

That the composite model event decays somewhat earlier than the *typical* El Niño as well as the *atypical* El Niños is probably related to several factors, including the nature of the mean climate state at the outset of the event and the strength of the anomalies that develop in the atmospheric and oceanic circulation. The interplay of these and other factors in determining the duration of a warm event in the GCM may be investigated in further diagnostic studies. The simulated atmospheric and oceanic anomalies are smaller than found in nature and suggest the possibility that the shorter duration in comparison with observations may be related to the weaker strength of the signal.

3. Mixed Layer Current Anomalies: Concomitant with the variation of SLP between the eastern Pacific and Indonesia is a mixed layer current variation due to the coupling of the ocean currents to the variation of the atmospheric forcing by windstress. During years of low Southern Oscillation Index the SLP gradient across the equatorial Pacific decreases, resulting in diminished Southeast trade winds. Firing *et al.* (1983), Wyrtki (1975, 1977) and Enfield (1981) have deduced from observations that a weakening of the South Equatorial Current occurs during El Niño resulting in an eastward transfer of warm water that is responsible for

the anomalous increase in SST in the central and eastern Pacific. Rasmusson and Carpenter (1982) have noted the development of anomalous equatorward flow in both hemispheres in the Pacific during a warm episode. The simulated anomalous ocean currents occur not only in the tropical Pacific basin but also in extra–tropical regions. The current anomalies are shown using velocity vectors of three different lengths; the smallest arrow is for speeds < 2cm s^{-1}, a medium arrow is for speeds ≥ 2cm s^{-1}but < 5cm s^{-1}, and the largest arrow is for speeds ≥ 5cm s^{-1}. It is interesting to note that the anomalies in equatorial flow converge near 115°W, 2°N, the grid–point noted earlier as having the strongest anti–correlation in SLP with the Indonesian region. The South Equatorial Current has been observed to reverse in direction, particularly in the western Pacific during El Niño years. The simulated anomalous atmospheric forcing of the currents is weaker than observed, recalling that the amplitude of the model Southern Oscillation Index is $\frac{1}{3}$ to $\frac{1}{2}$ that of the observed Southern Oscillation Index (Sperber *et al.* (1987). Hence the currents do not reverse; however the anomalies are in the observed direction. These eastward anomalies are supported by tropical flow converging to the equator from both hemispheres, as noted in the empirical observations of Rasmusson and Carpenter (1982).

The temporal evolution of the current anomalies during years of low Southern Oscillation Index can be evaluated by examining successive seasonal anomalies. It will be seen that the Pacific basin SST anomalies, given in Figure 1a–d, evolve roughly in parallel with the development of the current anomalies.

During spring, Figure 2a, eastward anomalies of 3–7.8cm s^{-1} are located in the equatorial region west of the dateline. The corresponding distribution of SST anomalies, given in Figure 1a, shows the highest SST anomalies in the same region. By summer, Figure 2b, the eastward equatorial Pacific anomalies west of 120°W and east of the dateline have increased in strength to 3–6cm s^{-1}. Concomitant with the expansion of equatorial eastward current anomalies is the spread of positive SST anomalies into the central/eastern Pacific Ocean. The distribution of SST anomalies in Figure 1b shows the central Pacific as the region of greatest warming. Northeastward flow from 8°S and 4°S in the longitude range 160°W to 130°W converges with the eastward equatorial current anomalies in the area of the largest positive SST anomalies. From the coast of South America to about 120°W westward anomalies of 2–6cm s^{-1}generally reinforce the climatological flow. These current anomalies are associated with westward expansion of eastern Pacific positive SST anomalies (clearly seen in the individual monthly composites). In the fall, Figure 2c, the eastward equatorial anomalies in the Pacific are highly developed with velocities of 5–11.7cm s^{-1}extending to nearly 120°W. The SST anomalies, Figure 1c, span the Pacific basin in conjunction with the well developed current anomalies. The equatorward flow in both hemispheres has increased relative to summer together with greater eastward current anomalies at the equator. In winter, Figure 2d, the current anomalies are highly organized. The eastward anomalies in the equatorial Pacific now range from 6–26cm s^{-1}. The strength of the equatorward current anomalies in both hemispheres has increased. Equatorward flow in the Pacific now comes from as far north as 16°N and as far south as 8°S, particularly west of the dateline. The waning of the positive SST anomalies precedes the decrease of eastward current anomalies in the model.

4. Discussion: Although we have concentrated our attention to the anomalous behavior in the Pacific basin, the simulated ocean currents throughout the globe depart from the mean state in a systematic fashion. The anomalous flow during low Southern Oscillation Index may be characterized in general terms: Flow in the tropical and southern regions of the Pacific, Indian, and Atlantic Oceans opposes the normal circulation; in the regions north of the tropics in the Pacific and Atlantic Oceans the current anomalies tend to augment the usual flow.

It should be noted that the simulated cold event (high phase of the Southern Oscillation) SST anomalies evolve in the same fashion but with the signs of the anomalies reversed, a known characteristic of the empirical data (Meehl, 1987; Kiladis and van Loon, 1988). During this phase the trans–Pacific pressure gradient is enhanced, resulting in mixed layer current anomalies in the tropical Pacific Ocean which augment the usual flow. Thus the cold event evolution is antithetical to that of the warm event.

Acknowledgement

This work was performed under the auspices of the U.S. Department of Energy by the Lawrence Livermore National Laboratory under contract W–7405–Eng–48.

References

Enfield, D. B., 1981: El Niño–Pacific eastern boundary response to interannual forcing. in *Resource Management and Environmental Uncertainty*, eds. M. H. Glantz and J. D. Thompson, Wiley, New York, 213–254.

Firing, E., R. Lukas, J. Sadler, and K. Wyrtki, 1983: Equatorial undercurrent disappears during 1982–1983 El Niño. *Science*, **222**, 1121–1123.

Kiladis, G. N., and H. van Loon, 1988: The southern oscillation. Part VII: Meteorological anomalies over the Indian and Pacific sectors associated with the oscillation. *Mon. Wea. Rev.*, **116**, 120–136.

Meehl, G. A., 1987: The annual cycle and interannual variability in the tropical Pacific and Indian Ocean regions. *Mon. Wea. Rev.*, **119**, 27–50.

Philander, S. G. H., 1983: El Niño Southern Oscillation phenomena. *Nature*, **302**, 295–301.

Rasmusson, E. M. and T. H. Carpenter, 1982: Variations in tropical sea surface temperature and surface wind fields associated with the Southern Oscillation/El Niño. *Mon. Wea. Rev.*, **110**, 354–384.

Sperber, K. R., 1989: *Southern Oscillation simulation in coupled ocean/atmosphere global climate models.*, Ph.D. Dissertation, State University of New York at Stony Brook, Stony Brook, NY, 157pp.

Sperber, K. R., S. Hameed, W. L. Gates, and G. L. Potter, 1987: Southern Oscillation simulated in a global climate model. *Nature*, **329**, 140–142.

Wyrtki, K., 1975: El Niño–the dynamic response of the equatorial Pacific Ocean to atmospheric forcing. *J. Phys. Oceanogr.*, **5**, 572–584.

Wyrtki, K., 1977: Sea level during the 1972 El Niño. *J. Phys. Oceanogr.*, **7**, 779–7871.

Figure Captions

Figure 1. Evolution of SST anomalies during simulated composite warm events. The contour spacing is 0.2°C. Contours $\geq$0.2°C are shaded. **a)** early spring(0) **b)** late spring/early summer(0) **c)** late summer/fall(0) **d)** winter(+1)

Figure 2. Evolution of mixed layer current anomalies during simulated warm events. **a)** spring(0) **b)** summer(0) **c)** fall(0) **d)** winter(+1)

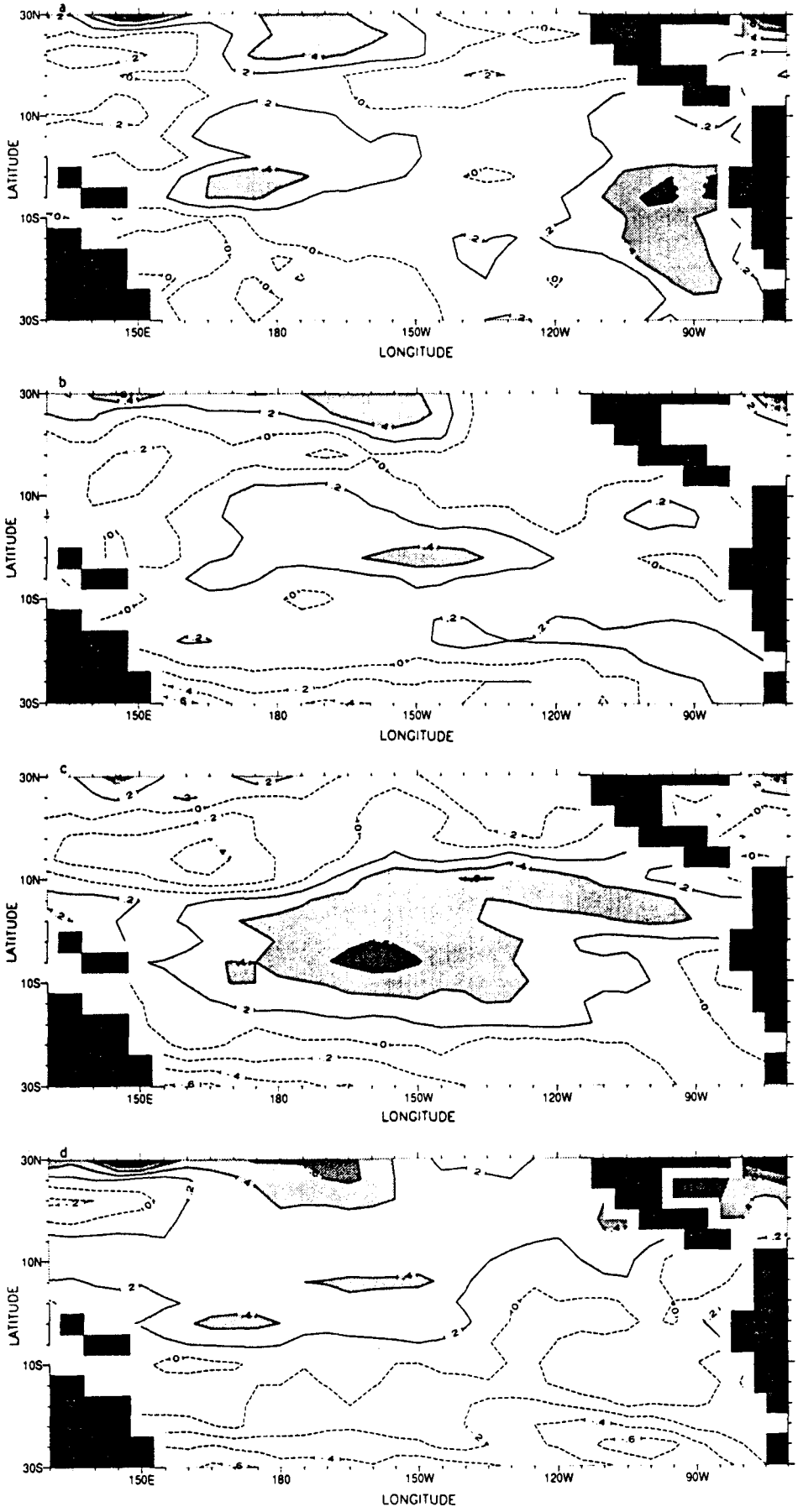
a
b
c
d
30N
10N
10S
30S
LATITUDE
150E
180
150W
120W
90W
LONGITUDE

Figure 1

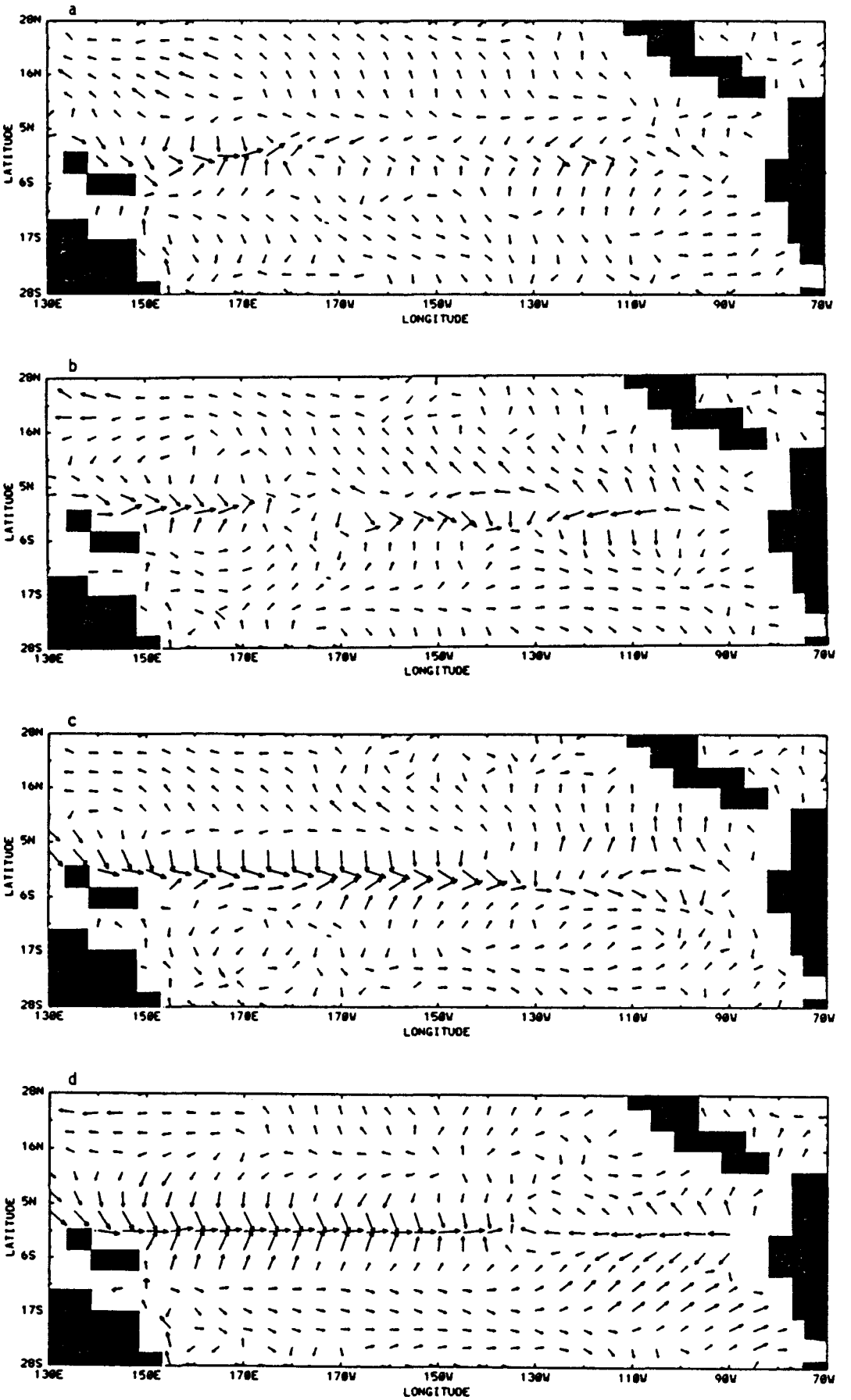
a
b
c
d
20N
16N
5N
6S
17S
20S
LATITUDE
130E
150E
170E
170W
150W
130W
110W
90W
70W
LONGITUDE

Figure 2